Journal of Rock Mechanics and Geotechnical Engineering 18 (2026) 4023–4033

Contents lists available at ScienceDirect

Journal of Rock Mechanics and Geotechnical Engineering

journal homepage: www.jrmge.cn

Full Length Article

Visualizing enzyme-induced mineralization in fractures

Yang Xiao [a], Chang Zhao [a,*], Qingyun Fang [a], Xiang He [b], Jian Chu [b], Hanlong Liu [a]

[a] Key Laboratory of New Technology for Construction of Cities in Mountain Area, Chongqing University, Chongqing, 400045, China
[b] School of Civil and Environmental Engineering, Nanyang Technological University, 639798, Singapore

ARTICLE INFO

Article history:
Received 5 March 2025
Received in revised form
2 June 2025
Accepted 2 June 2025
Available online 17 September 2025

Keywords:
Enzymatically Induced Carbonate Precipitation (EICP)
Fracture healing
Fracture roughness
Fracture aperture
Visualization method
Permeability evolution

ABSTRACT

Effective sealing of geological fractures is essential for subsurface stability and mitigating environmental risks such as groundwater contamination and inefficient CO_2 sequestration. Enzymatically Induced Carbonate Precipitation (EICP) offers a promising bio-mediated approach due to its ability to fill and seal fractures. However, real-time precipitation patterns and clogging behavior of EICP under varying fracture and flow conditions remain poorly understood. This study employs a transparent fracture model with visualization to systematically investigate the effects of fracture aperture, flow conditions, and surface roughness on EICP-mediated sealing. Results indicate that fractures with narrower apertures promote tortuous finger-like flow paths, while wider-aperture fractures show more uniform deposition, with fewer but wider preferential flow paths. An appropriate injection rate around 1 mL/min ensures uniform precipitation and effective clogging, avoiding inlet clogging at lower rates (0.1 mL/min) and flushing effect reducing deposition at higher rates (10 mL/min). Additionally, rough fractures exhibit higher precipitation efficiency and greater permeability reduction, driven by their irregular surface geometry, which creates more deposition sites and complex flow compared to smooth fractures. Image processing reveals that precipitation patterns in rough fractures match closely with aperture distribution, compared to more concentrated deposition in smooth fractures. These findings provide insights for optimizing EICP-mediated fracture sealing, with implications for groundwater protection and geotechnical practices.

1. Introduction

Remediation of fractured rock is a critical challenge in geotechnical and environmental engineering. Subsurface rock fractures can pose a serious risk to the structural integrity of geological formations, leading to potential groundwater contamination and inefficient CO_2 sequestration processes (Viswanathan et al., 2022). Traditional methods for fracture repairing usually involve invasive mechanical techniques or the injection of chemical grouts, which could pose environmental risks and long-term stability issues (da Rocha Gomes et al., 2023). Biomineralization is widely recognized as a critical process in geological sedimentation (Boquet et al., 1973). In recent years, bio-mediated techniques, particularly Microbially or Enzymatically Induced Carbonate Precipitation (MICP or EICP), have emerged as promising alternatives (Xiao et al., 2022a), which have shown significant potential in soil solidification (Zhao et al., 2020; Lai et al., 2023a; Cui et al., 2024), liquefaction resistance (Xiao et al., 2018, 2019; Hu et al., 2024), and slope stability (Xiao et al., 2022b). These techniques offer advantages such as low viscosity, good flowability, and efficient reinforcement, making them particularly effective in repairing microfractures (Alarifi et al., 2022). EICP, in particular, utilizes urease enzymes to hydrolyze urea, resulting in $CaCO_3$ precipitation that can fill and seal fractures. Previous studies have demonstrated the potential of the bio-mediated method for fracture healing across various scales (Song et al., 2024). At the microscale, researchers have utilized microfluidic technology to observe the nucleation and growth of biological carbonate minerals within porous media (Wang et al., 2019a, b; Zhang et al., 2025). These studies have revealed that the distribution and morphology of precipitates are influenced by factors such as concentrations (Wang et al., 2021; Xiao et al., 2022c), flow velocity (Zhao et al., 2023), and mineralization types (Xiao et al.,

* Corresponding author.
E-mail address: zhaochangchn@163.com (C. Zhao).

Peer review under responsibility of Institute of Rock and Soil Mechanics, Chinese Academy of Sciences.

https://doi.org/10.1016/j.jrmge.2025.06.035

2024). For instance, Weinhardt et al. (2021) investigated the formation of calcite in a microfluidic cell, highlighting the significant reduction in permeability due to the deposition of $CaCO_3$ within narrow pore throats. Zhao et al. (2025a, b) examined the impact of injection strategies and concentrations on EICP process within microchannels and found that a one-phase staged injection strategy and appropriate concentrations of urease and cementing solution demonstrated good precipitation efficiency. The microscale interactions of enzymatically induced $CaCO_3$ on rock surfaces were observed in rock-based chips to study the clogging effect (Xiao et al., 2025). These microscale experiments offered valuable insights for optimizing biogrouting techniques at larger scales.

At the macroscale, many studies have validated the effectiveness of the biogrouting technique for repairing rock fractures. Tobler et al. (2018) observed the formation and bonding of calcite at rock interfaces, which resulted in approximately three orders of magnitude reduction in permeability with 41 % of the fracture volume occupied by calcite. In experiments involving MICP method on naturally weathered rough fractures, Dong et al. (2022) found that $CaCO_3$ deposition was more pronounced at the convexities of fractures due to high bacterial adsorption. Wu et al. (2019a, b, c) conducted a series of one-dimensional and two-dimensional MICP experiments to analyze the influence of fracture aperture and flow dynamics on precipitation behavior. Their findings indicated that the accumulation of precipitates led to a transition from surface flow to channel flow within the fractures (Wu et al., 2019c). Field studies further demonstrated the potential of biogrouting in controlling subsurface fracture permeability and clogging. Previously, Cuthbert et al. (2013) applied MICP grouting through borehole injections into subsurface fractures, showing a marked decrease in transmissivity of a fracture several-square-meter in size after about 17 h of treatment. Additionally, Phillips et al. (2016) successfully employed biogrouting to remediate leakage pathways near wellbores, achieving a 75 % reduction in injectivity due to clogging. However, these studies primarily concentrated on the eventual macroscale performance of bio-treated fractures, treating the process as a "black box" that does not allow for real-time experimental visualization. To investigate real-time precipitation behaviors at the macroscopic level, several researchers such as Minto et al. (2016) and Liu et al. (2024) employed time-lapse photography to track the distribution of $CaCO_3$ on granite surfaces, and the progression of fracture sealing via MICP grouting. In a related study on polycarbonate fractures, EI Mountassir et al. (2014) observed the development of self-organized channels, attributed to interactions between hydrodynamics and biocementation. However, polycarbonate does not adequately represent geomaterial properties, and its imaging resolution is limited. Moreover, while many studies have focused on MICP for fracture healing, EICP potentially offers greater advantages for sealing microfractures (Alarifi et al., 2022). Firstly, EICP does not require the use of exogenous bacteria, reducing potential risks in field applications. Secondly, the size of the urease enzyme, approximately 12 nm, is significantly smaller than that of bacteria (0.5−5 μm) (RAN and Kawasaki, 2016). This allows the enzyme to penetrate microfractures and pores more effectively, making it suitable for micro-fracture healing. This study employed advanced visualization methods, including high-resolution imaging and time-lapse photography, to examine the EICP method for sealing fractures in a transparent glass model. It investigated the impact of fracture aperture and injection rates on bioclogging in both smooth and rough fractures, revealing distinct precipitation patterns. As aperture increases (0.18−2 mm), preferential flow paths shift from numerous narrow channels to fewer, wider ones, resulting in significant clogging and reasonable precipitation efficiency. Extremely low and high injection rates were found to be unsuitable for achieving uniform precipitation and effective bioclogging. The results indicate that rough fracture apertures closely match the precipitation distribution. This research offers insights for improving EICP applications for sustainable and effective fracture remediation.

2. Experimental details and testing procedure

The visual reaction platform used in this study, which expands on our previous microfluidic research (Zhao et al., 2025a; Xiao et al., 2025), allows for real-time visualization of the EICP reaction process at the macroscale. It comprises four main components: an optical imaging system, an injection system, data acquisition units, and a fracture model, as illustrated in Fig. 1a. A high-resolution industrial camera (Hikvision GE2000MRC-T1-C3) was installed above the fracture model. An LED light source was placed below the model to enable light transmission through the transparent fracture, allowing real-time imaging of the precipitation process every 10 min. Syringe pumps (Harvard Apparatus, Pump 11 Elite, USA) were utilized to inject the reactive solutions at a constant rate. The data acquisition units include a pressure unit (Fluigent, EIPS7000) to measure fluid pressure and a computer to save the captured images. The fracture model consists of two transparent rectangular glass plates (20 cm × 10 cm). Glass was chosen for its transparency and silicon-based composition, which closely mimics the mineral composition of natural rocks. Two types of fractures were used in this study: a smooth fracture, made of two smooth glass plates, and a rough fracture, made of one rough bottom glass plate and one smooth glass plate. Glass beads of varying sizes were placed between the two glass plates to create fractures with varying apertures. Poly(methyl methacrylate) (PMMA) was used to hold the glass plates in place, and silicon glue was applied to seal the model and prevent leakage. The schematic graph of the fracture model is shown in a magnified view in Fig. 1a. The inlet PMMA was drilled with a hole to connect the injection tube, while the outlet PMMA was drilled with three holes to connect tubes to allow fluid to flow out. In smooth fractures, the aperture is uniformly distributed, whereas in rough fractures, it is heterogeneously distributed.

To determine the fracture aperture field in a rough fracture, the mean fracture aperture is measured using the mass conservation method (Neretnieks, 2007). This involves measuring the masses of two glass plates before and after filling with deionized water to obtain the mass difference (Δm). The mean mechanical fracture aperture ($\langle b \rangle$) is then calculated as $\langle b \rangle = \Delta m/(\rho_w WL)$ (Chen et al., 2024), where ρ_w is the density of water, W and L are the fracture width and length, respectively. The results of mean fracture aperture are shown in Table 1. To visualize aperture distribution, dyed water was injected into the rough fracture to saturate the whole chamber. Regions with wider apertures absorb a greater proportion of light, resulting in a darker appearance under light transmission. According to the Beer-Lambert law, the proportion of light absorbed by each equal layer is constant, regardless of the initial intensity of the light. Thus, the transmitted light intensity (I) passing through the solute solution can be expressed as $I = I_0 e^{-\mu Cb}$ (Detwiler et al., 1999), where I_0 represents the incident light intensity. μ represents the absorptivity of the solute, C is the concentration of the solute. Using this relationship, we can indirectly determine the aperture at each pixel, more details can be found in a previous study (Chen et al., 2024). Finally, an iterative process is applied to calculate the mean mechanical aperture across the fracture, adjusting until the calculated mean aperture ($\langle b \rangle_{\mathrm{cal}}$) is close to the measured mean aperture ($\langle b \rangle$), meeting the condition (Chen et al., 2024) of $|(\langle b \rangle - \langle b \rangle_{\mathrm{cal}})/\langle b \rangle| \leq \delta$, where the tolerance of δ is set to 0.01. The calculated mechanical aperture distribution of

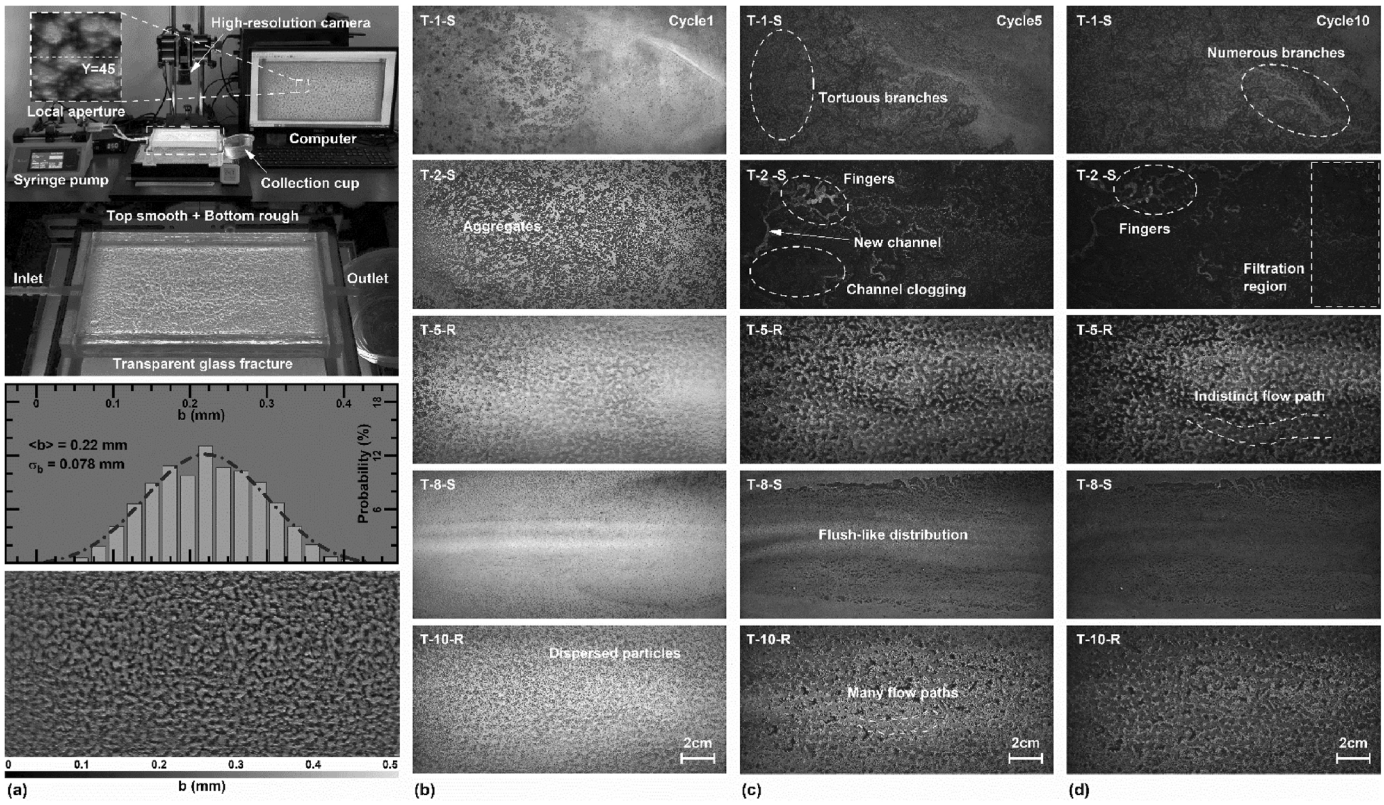

Fig. 1. (a) Diagram of the transparent fracture-visualization platform (adapted from Xiao et al. (2025)) and characterization of the initial fracture aperture field. Precipitation patterns in representative experiments at stages of (b) Cycle 1, (c) Cycle 5, and (d) Cycle 10.

Table 1
Experimental conditions and calculating results for transparent fracture repairing.

No.	$\langle b \rangle$ (mm)	Q (mL/min)	T (min)	m_c (g)	ϕ_c^N (%)	Φ (%)	Ω
T-1-S	0.18	1	7	1.6	16.4	16.4	0.683
T-2-S	0.5	1	20	4.1	15.1	14.7	0.492
T-3-S	1	1	35	10.1	18.6	20.7	0.057
T-4-S	2	1	60	18.9	17.4	22.6	0.029
T-5-R	0.22	1	7	2.0	16.8	20.5	0.58
T-6-R	1.22	1	35	13.7	20.8	28.2	0.019
T-7-S	0.18	0.1	70	2.3	23.8	29.7	0.014
T-8-S	0.18	10	0.7	2.3	23.6	23.6	0.875
T-9-R	0.22	0.1	70	2.6	22.2	30.2	0.011
T-10-R	0.22	10	0.7	2.7	22.6	27.7	0.818

Notes: S and R denote smooth fracture and rough fracture, respectively.

the narrow rough fracture is shown in Fig. 1a, with an average mechanical fracture aperture of 0.22 μm following a Gaussian distribution. For the rough fracture with a wider aperture, 1 mm glass beads were embedded, forming an aperture of approximately 1.22 mm.

An equimolar concentration of 1 M $CaCl_2$ and urea was utilized as the cementing solution. The urease enzyme solution was extracted from soybean seeds following the protocols outlined in previous studies (Lai et al., 2023b; Zhao et al., 2024). Initially, the soybeans were ground into a fine powder and sieved to obtain particles smaller than 0.18 mm. The resulting powder was stored at 4 °C to preserve enzyme activity. A slurry was prepared by mixing the soybean powder with deionized water to achieve a concentration of 100 g/L, followed by stirring with a magnetic stirrer for 0.5 h. Subsequently, the mixture was filtered through a No. 300 mesh to remove larger impurities and centrifuged at 4000 rpm for 0.5 h at 4 °C. The supernatant was filtered again to remove remaining solid residues. The prepared enzyme solution was then stored at 4 °C prior to use. The electrical conductivity method was employed to measure the enzyme activity of the urease solution (Whiffin, 2004). Specifically, 2 mL of the urease solution was added to 18 mL of a 1.1 M urea solution, and the changes in electrical conductivity were monitored over a 5-min period at 20 °C. The resulting urease activity was adjusted to approximately 6.5 mM of urea hydrolyzed per minute for subsequent experiments. Four fracture apertures ($b = 0.18$ mm, 0.5 mm, 1 mm, 2 mm) were used in the smooth fracture, and two apertures ($\langle b \rangle = 0.22$ mm, 1.22 mm) were used in the rough fracture to investigate the influence of fracture aperture on precipitation behaviors. Three different total flow rates ($Q = 0.1, 1, 10$ mL/min) were applied in both smooth and rough fractures to study the impact of flow rates on precipitation behaviors. The Reynolds number was adopted to evaluate the flow patterns within fractures (Zimmerman et al., 2004), calculated as $\mathrm{Re} = v_{\mathrm{flow}}\langle b \rangle/\nu$, where v_{flow} is the flow velocity, and ν is the kinematic fluid viscosity. The values of Re ranged from 0.02 to 1.67, indicating laminar flow within the fracture cell. The experiments employed a one-phase staged injection strategy (Lai et al., 2023b). In each cycle, the soybean enzyme solution and cementing solution were injected simultaneously into the transparent fracture at a constant flow rate, ensuring the fracture chamber was completely filled. Each experiment featured different flow rates (Q) and injection periods (T), as detailed in Table 1. Following the injection, the system was left to stand for approximately 8 h to allow for EICP reactions. Each experiment consisted of a total of 10 treatment cycles. The captured grayscale images were initially cropped to obtain a rectangular area of 19 cm × 9 cm to minimize the impact of uneven edge illumination, and the resulting resolution was approximately 40 μm/pixel. The presence of precipitates within the fracture can

impede light transmission, resulting in changes to the grayscale values. A previous study utilized image intensity to evaluate precipitation content (Minto et al., 2016). Following our prior analytical method (Zhao et al., 2025a), the density of image intensity (int.) is calculated as the ratio of the sum of grayscale values within a selected region to the pixel area of that region. After EICP treatment, the fracture model was disassembled and the samples were dried at 80 °C for 48 h prior to acid washing. Subsequently, the transparent plates were opened, and the distribution of $CaCO_3$ deposits was photographed for analysis. Selected samples with minimal deposition were examined under a Quattro Environmental Scanning Electron Microscope (ThermoFisher, USA) to observe the morphology of the $CaCO_3$ crystals.

After each treatment cycle, deionized water was injected into the fracture at a flow rate of 0.5 mL/min for a while. A pressure unit was installed in the injection tube to measure the inlet pressure, while the outlet, directly connected to the air, was assumed to be at atmospheric pressure. Based on the obtained pressure differences (Δp), the permeability coefficient of fracture (K) due to precipitation clogging can be calculated by Darcy's law (Dullien, 1992), expressed as: $K = QL\rho_w g/(A\Delta p)$, where Q is the flow rate, which is 0.5 mL/min. g is the gravitational acceleration, A is the cross-sectional area of the fracture, calculated as $A = W \times \langle b \rangle$. During the permeability measurement via water injection, the effluent of the reactive solution within the fracture chamber was collected. The concentration of residual calcium ions in the effluent was determined using the disodium ethylenediaminetetraacetic acid (EDTA-2Na) titration method (Choi et al., 2017). The precipitation efficiency (E_c^n) during the n-th treatment cycle was estimated as $E_c^n = (1 - C_{Ca^{2+}}^{effl}/C_{Ca^{2+}}^{mix,0}) \times 100\%$ (Cui et al., 2022), where $C_{Ca^{2+}}^{effl}$ is the concentration of calcium ions in the effluent, and $C_{Ca^{2+}}^{mix,0}$ is the concentration of calcium ions in the initial mixed solution (0.5 M). After completing all injection processes, the fracture model was demolded and thoroughly rinsed with a 1 M HCl solution for 24 h to ensure complete dissolution of $CaCO_3$. The total concentration of calcium ions in the acid solution ($C_{Ca^{2+}}^{tot}$) was then measured to determine the $CaCO_3$ mass ($m_c = C_{Ca^{2+}}^{tot} \cdot V_{acid} \cdot M_c$) and $CaCO_3$ content ($C_c = m_c/(\rho_c \cdot W \cdot A) \times 100\%$). The real total precipitation efficiency (E_c^{real}) within fractures can be obtained as $E_c^{real} = C_{Ca^{2+}}^{tot} \cdot V_{acid}/(C_{Ca^{2+}}^{mix,0} \cdot Q \cdot T \cdot N) \times 100\%$, where M_c is the molar mass of $CaCO_3$, V_{acid} is the volume of acid solution, T is the duration of each injection, and N is the total numbers of treatment cycles. By analyzing the E_c^n values in each cycle, we can calculate the ideal total precipitation content, and determine the ideal precipitation efficiency (E_c^{ideal}) as the ratio of actual to ideal $CaCO_3$ content, calculated as $E_c^{ideal} = C_{Ca^{2+}}^{tot} \cdot V_{acid}/(C_{Ca^{2+}}^{mix,0} \cdot Q \cdot T \cdot \sum_1^n E_c^n) \times 100\%$.

3. Experimental results and interpretations

The precipitation patterns were captured at different moments, some representative experiments are shown in Fig. 1b–d, and more details can be found in Figs. A1 and A2 and supporting videos in Appendix A. For T-1-S (b0.18-Q1), when the soybean enzyme solution and cementing solution were introduced, irregular flocs formed and entered the fracture channel with a parabolic shape. These flocs appeared dark due to blocking light transmission and were carried by the flow. During the 1st injection, the flocs tended to settle under gravity when the injection paused, while barely visible particles became lighter after the fresh reactive solution supply ceased. This phenomenon aligns with previous microscale observations (Zhao et al., 2025a, b) and is likely due to the formation and dissolution of ACC (amorphous calcium carbonate), which dissolves to support the growth of $CaCO_3$ crystals (Wang et al., 2019a). In the 2nd injection, the flocs shifted location and formed numerous tortuous branches in the front of the fracture (Fig. A1 in Appendix A), gradually expanding to cover the entire fracture. As injection cycles continued, some channels were rearranged while others were self-reinforced by the flow behavior, a phenomenon also observed in previous biogrouting tests conducted in smooth polycarbonate fractures (Mountassir et al., 2014). As the fracture aperture increased (T-1–4) at the same injection rate, the flocs became larger and darker due to their increased thickness, as shown in Fig. A1 in Appendix A. In T-2-S ($b = 0.5$ mm), a preferential flow path developed during the 3rd cycle, as seen in Video A1 in Appendix A. As the fracture narrows, the fluid pressure acting on the precipitates increases, making them more susceptible to transport. By the fourth cycle, a high concentration of newly formed $CaCO_3$ precipitated in the existing path, clogging it and redirecting flow to form new channels and finger flows. This phenomenon was also observed in previous visualizations of MICP sealing fine fractures (Liu et al., 2024), along with the formation of filtration zones at the rear end of the fracture. This phenomenon was also observed in previous bio-grouted sandstone tests (Minto et al., 2017). It should be noted that the rigid fracture model constrains any aperture deformation. However, in field applications, high fluid pressures may cause fracture dilation, potentially reducing EICP sealing efficiency, which requires further investigation. In fractures with wider apertures ($b = 2$ mm), the preferential flow path is less apparent due to thick precipitates blocking light. Additionally, the lower flow velocity in wider apertures led to significant aggregation near the inlet. Over time, precipitates gradually fill the fracture channels. The rough fracture exhibited different behavior compared to the smooth fracture due to its uneven bottom surface. In T-5-R (b0.22-Q1), concave areas with wider apertures retained more precipitates under lower flow velocity. Irregular substances formed in convex areas during injection but disappeared during the subsequent standing period, as shown in Video A2 in Appendix A. This can be explained by the relatively faster precipitation rates that tend to occur in convex regions under fluid dynamics, as indicated in a previous study (Dong et al., 2022), leading to rapid formation of ACC. Precipitation increased with each treatment cycle. A preferential flow path also formed in the rough fracture with $b = 0.22$ mm, though it was less pronounced compared to the smooth fracture. The distribution of precipitates was uneven due to the irregular aperture field. However, in T-6-R (b1.22-Q1), roughness had little effect in wider apertures. A wide preferential flow path formed in the first cycle but became clogged in the second, followed by the creation of a new flow path (as seen in Video A3 in Appendix A). The fracture was nearly filled with precipitates in later cycles, exhibiting an overall uniform precipitation distribution. Flow rates significantly affect precipitation behavior. At a low flow rate ($Q = 0.1$ mL/min), only small, spot-like particles formed within the smooth fracture, with the formation and dissolution of amorphous substances observed. In subsequent treatment cycles, a greater quantity of precipitates was observed near the inlet. However, the total amount of precipitates was lower compared to the flow rate of 1 mL/min. In fact, after demolding from the low-flow test, evident precipitation clogging was detected within the inlet chamber. This phenomenon occurred because the rapid and substantial generation of precipitates accumulated at the inlet before they could be transported into the fractures. In contrast, a high flow rate ($Q = 10$ mL/min) resulted in a distinct flush-like distribution, with fewer precipitates in the center and more along the sides due to the flushing effect. A similar pattern was observed in previous MICP visualizations in smooth fractures (Minto et al., 2016). In rough fractures (Fig. 1b–d and Fig. A1 in

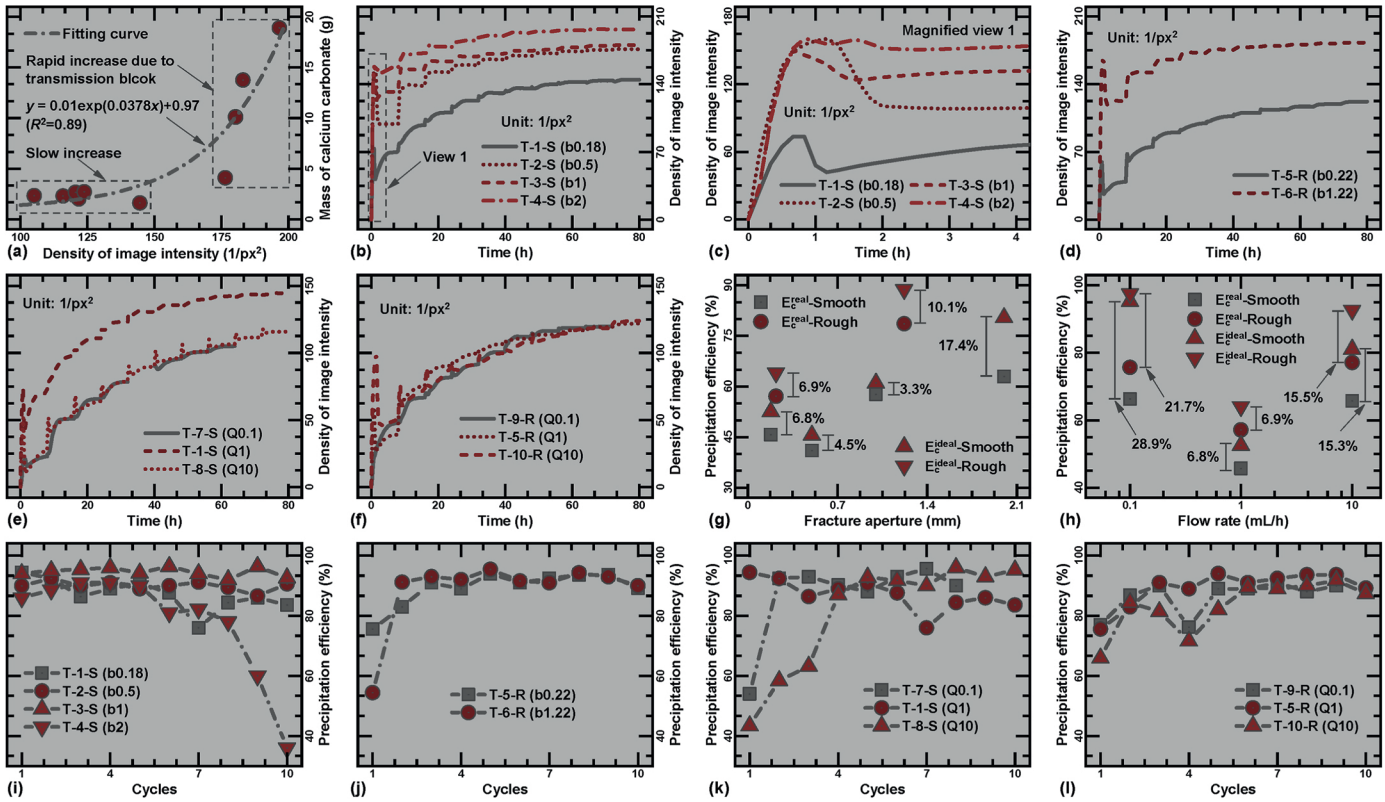

Fig. 2. Global precipitation evaluation and precipitation efficiency: (a) Relationship of m_c and int, (b)–(f) Evolution of int. over time, (g)–(h) Relationship of E_c^{real} and E_c^{ideal} fracture aperture and flow rate, and (i)–(l) Evolution of E_c over treatment cycles.

Appendix A), precipitates initially resembled the aperture field but later formed more aggregates, reducing inlet clogging compared to smooth fractures. At extremely high flow rates, more small particles were deposited within the fracture, with some precipitates accumulating in concave regions, which could lead to preferential flow paths, as discussed later.

As previously described, the density of image intensity was used to assess the amount of precipitation. The final precipitation mass (m_c) was measured precisely, and the relationship between the final values of int. and m_c is shown in Fig. 2a. It can be observed that the mass of precipitates increases exponentially with the rise in density of image intensity. This is consistent with results from previous microscale experiments (Zhao et al., 2023), which showed a similar trend between the precipitation volume fraction and image density. When the precipitate mass exceeds a certain level (over 5 g in this study), a significant increase in int. is observed, likely due to the obstruction of light transmission by the accumulated precipitates. Fig. 2b–f demonstrates the evolution of int. over time across all experiments. All cases show a stepwise increase corresponding to the treatment cycles. Regardless of the fracture aperture, as shown in Fig. 2b–d, both smooth and rough fractures showed a sharp rise in int. during injection, which continues briefly after injection stops, followed by a notable drop within 1 h. As the fracture aperture increases, the fluctuations during the 1st cycle become less pronounced, likely due to the reduced flow velocity in wider apertures. It is hypothesized that low flow velocities were not conducive to ACC formation, as evidenced in Fig. 2e–f, where the fluctuation trend of int. is less pronounced at $Q = 0.1$ mL/min compared to $Q = 10$ mL/min. For apertures ranging from 0.18 mm to 2 mm, the final values of image density span from 144 to 197 1/px^2, while the final precipitation mass ranges from 1.6 to 18.9 g (Table 1). This suggests that even a small amount of precipitation can hinder light transmission, resulting in high int. values at low precipitation mass. Additionally, both extremely high and low flow rates are not favorable for precipitation clogging, as indicated by the lower final int. values compared to $Q = 1$ mL/min in smooth fractures, and similar int. values in rough fractures. High flow rates also tend to promote the appearance and dissolution of irregular substances, which has been explored in previous microfluidic studies (Xiao et al., 2025). The precipitation efficiency after each cycle was measured, and the results are shown in Fig. 2i–l. In smooth apertures (Fig. 2i), the experiments demonstrated a high precipitation efficiency, exceeding 80 %, except for the case where $b = 2$ mm, which showed a decreasing E_c over nine cycles, reaching 36 % by the 10th cycle. This reduction may be due to significant clogging within the fracture cell, where the injected solution may not be sufficient for complete reaction. The precipitation efficiency in rough fractures remained high throughout each cycle, except for the first cycle in T-6-R-b1.22-Q1 (Fig. 2j). Additionally, both extremely low and high flow rates in smooth fractures result in low precipitation efficiency during the initial treatment cycles, especially at higher flow rates (Fig. 2k). High flow rates tend to promote frequent mass transfer, where advection dominates over diffusion. In this scenario, precipitation more easily reaches supersaturation, leading to rapid ACC formation (Mukhopadhyay and Dalvi, 2005), which inhibits the growth of ordered crystals, as observed in earlier microscale studies (Xiao et al., 2025). Under high flow shearing forces, many precipitates fail to adhere to the fracture surface, reducing the possibilities for heterogeneous nucleation. As a result, the value of E_c is low initially, but increases in later cycles as more precipitates deposit on the surface, providing additional secondary nucleation sites (Lioliou et al., 2007). In rough fractures (Fig. 2l), the initial low efficiency is less pronounced compared to smooth fractures,

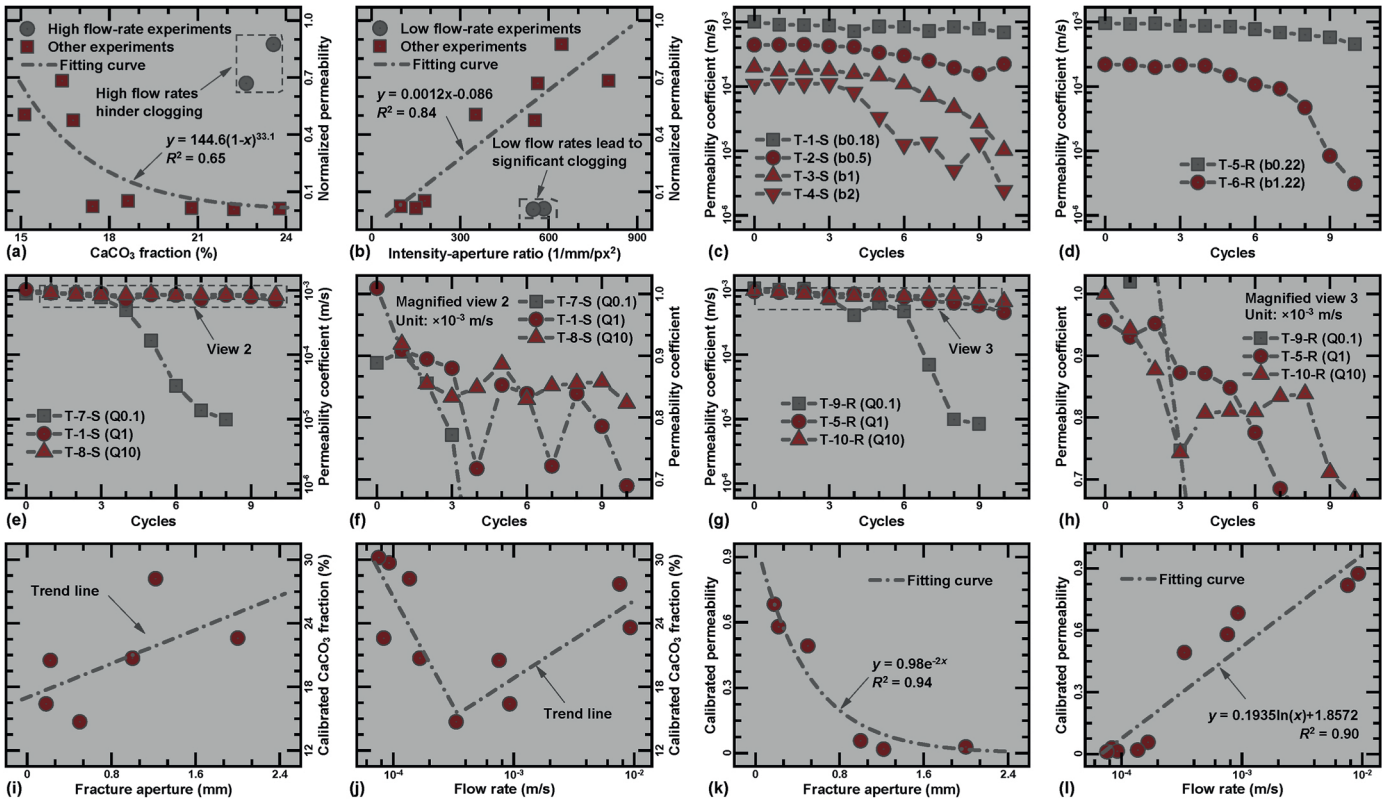

Fig. 3. Hydraulic performance of EICP healing fractures: (a) Relationship of K_N/K_0 and ϕ_c^N, (b) Relationship of K_N/K_0 and int./$\langle b \rangle$, (c)–(h) Evolution of K over treatment cycles, (i)–(j) Relationship of Φ with fracture aperture and flow rate, and (k)–(l) Relationship of Ω with fracture aperture and flow rate.

possibly because the uneven flow in rough fractures enhances mixing and promotes precipitation reaction. The ideal precipitation efficiency (E_c^{ideal}) for each treatment cycle and the real efficiency (E_c^{real}) based on the final precipitate mass were also calculated. It is observed that the values of E_c^{ideal} and E_c^{real} are inconsistent. This discrepancy is attributed to the loss of precipitates caused by flow displacement during the injection process and permeability measurement. Fig. 2g shows the effect of fracture aperture on precipitation efficiency. It can be observed that in smooth fractures, the efficiency initially decreases slightly and then increases as the fracture aperture widens. In rough fractures, wider-aperture fractures result in higher E_c values compared to narrower-aperture ones. Fractures with wider apertures are typically associated with greater efficiency differences, reaching 17.4 % at $b = 2$ mm, which aligns with the test results reported by (Wu et al., 2019c). This could be attributed to lower flow velocities within the fracture cell, a phenomenon that is more pronounced at $Q = 0.1$ mL/min, where the efficiency differences reach 28.9 % and 21.7 % in smooth and rough fractures, respectively (Fig. 2h). As flow rates increase, E_c first decreases and then rises. This finding differs from previous outcomes (Wu et al., 2019c), where precipitation efficiency was found to decrease with increasing flow velocity. The discrepancy may be due to the fact that only about one fracture volume of reactive solution was injected at varying flow rates, unlike other studies that maintained a constant injection period. After a standing period, the final precipitation mass at high flow rates is greater due to the enhanced mixing effect during injection, resulting in improved precipitation efficiency.

The fracture permeability coefficient (K) was calculated and presented in Fig. 3c–h. Regarding the effect of fracture aperture, Fig. 3c–d shows that at fractures with narrow apertures, the reduction in permeability is less pronounced, with decreases of 31.7 % in T-1-S (b0.18-Q1) and 42.0 % in T-5-R (b0.22-Q1). As the aperture increases, the clogging effect becomes more significant. For instance, when the aperture exceeds 1 mm, the value of K decreases by 94.3 % in T-3-S (b1-Q1) and 98.1 % in T-6-R (b1.22-Q1). At an aperture of 2 mm, K drops by 97.15 % after 10 treatment cycles, with fluctuations observed in later cycles, possibly due to the formation of new preferential flow paths. The significant reduction at wide apertures is likely due to the gradual blockage of fine flow channels (Liu et al., 2024). In contrast, narrower fractures show smaller reductions in permeability, as more flow fingers are difficult to fully fill with precipitates. Additionally, bioclogging is more effective in rough fractures compared to smooth ones, as uneven surfaces provide more low-flow velocity zones for $CaCO_3$ deposition (Peng et al., 2020). Regarding the impact of flow rates on permeability evolution, Fig. 3e–h shows that under extremely low flow rates, a rapid decrease in K is observed starting from cycle 4 in the smooth fracture (T-7-S-b0.18-Q0.1), resulting in a final reduction of 98.6 %. A similar trend is observed in the rough fracture (T-9-R-b0.22-Q0.1), where the permeability begins to decline rapidly from cycle 6, with a drop of two orders of magnitude. However, only a small amount of precipitate is visible during reaction. The image density and final precipitate mass are similar to those observed under the T-1-S condition. This discrepancy may be due to clogging at the inlet, which has been confirmed in previous studies showing slow injection rates tend to cause such clogging. Furthermore, an extremely high injection rate ($Q = 10$ mL/min) is also ineffective at reducing fracture permeability, performing worse than $Q = 1$ mL/min, with K reductions of 20 % in smooth fractures and 26 % in rough fractures. In light of this, the relationship between K_N/K_0 and the final precipitation volume fraction (ϕ_c^N) is shown in Fig. 3a. It is evident that high flow-rate injections are not conducive to precipitation clogging,

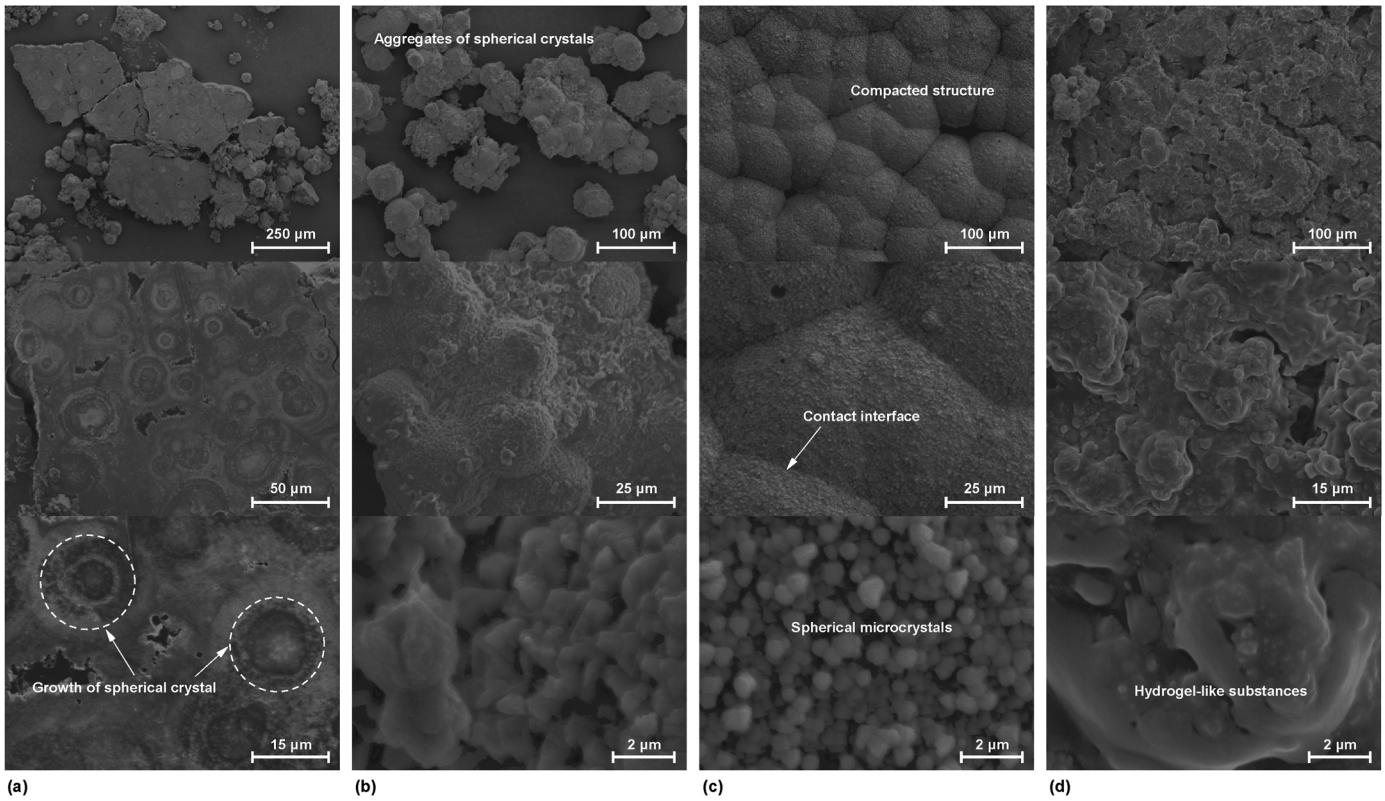

Fig. 4. Microscopic characterization of biological precipitation for smooth fractures with different apertures based on SEM images: (a)–(b) T-2-S (b0.5-Q1), (c) T-3-S (b1-Q1), and (d) T-4-S (b2-Q1).

resulting in a minimal permeability reduction. Apart from these cases, the value of K_N/K_0 tends to decrease as ϕ_c^N increases. A sharp reduction in permeability occurs when ϕ_c^N reaches a critical value of 17.4 %, leading to over a 90 % reduction in permeability. Previous MICP sealing fracture tests also exhibit significant variability (Wu et al., 2019b). This may be attributed to the dynamic evolution of the precipitation pattern, which can significantly influence flow behavior. We also employed parameter of the intensity-aperture ratio (int./$\langle b \rangle$) to estimate precipitation content. However, permeability reduction increases with int./$\langle b \rangle$, except in the low flow-rate experiments (Fig. 3b). This result contrasts with the findings based on precipitation volume fraction, likely because int. is insufficient to accurately reflect precipitation content in wide fractures due to light-blocking effects. The direct use of ϕ_c and K values does not accurately reflect the true impact of fracture aperture and flow rates on the precipitation clogging effect, as the volume of reactive solution applied varies across different experiments. Therefore, the experiment of T-1-S was taken as standard injection case. For the other k-th experiments, a calibrated factor (η_k) was introduced to measure the injection volume of the reactive solution relative to the fracture volume, expressed as $\eta_k \propto Q_k \cdot T_k \cdot N_k / \langle b \rangle_k$. Thus, the injection-volume-calibrated $CaCO_3$ fraction (Φ) was calibrated as $\Phi = \phi_N^c / (\eta_k / \eta_1)$, and the calibrated permeability coefficient (Ω) was calibrated as $\Omega = K_N/K_0/(\eta_k/\eta_1)$. The values of Φ and Ω are presented in Table 1, and more calculation details can be found in Table A1 in Appendix A. The effects of fracture aperture and flow rates are illustrated in Fig. 3i–l. Regarding the impact of fracture aperture (Fig. 3i and k), the precipitation volume fraction slightly increases as the aperture expands, while the injection-volume-calibrated permeability reduction decreases exponentially. This can be attributed to the lower flow velocities and smaller shear forces in wider apertures, which promote $CaCO_3$ nucleation and crystal growth. As for the effect of flow rates, Fig. 3j revealed an initial decrease followed by an increase in the calibrated ϕ_c^N, while Fig. 3l showed an increasing trend in K_N/K_0 as the fracture aperture enlarged. Low flow rates can result in high precipitation volume fractions, but may also cause inlet clogging under one-phase injection strategy (Handley-Sidhu et al., 2013). While this is beneficial for reducing permeability, it is not ideal for overall precipitation improvement, particularly in large-scale fracture healing scenarios. Conversely, excessively high injection rates generate significant shear forces, which can negatively impact nucleation and precipitation behavior, thus hindering the reduction of permeability, consistent with previous EICP experiments using the prehydrolysis method (Zhu et al., 2023). Overall, an injection rate of approximately 1 mL/min (resulting in a flow velocity of ~1 mm/s) was found optimal, as it balances advection and diffusion to promote uniform $CaCO_3$ deposition across the fracture, minimizing inlet clogging observed at 0.1 mL/min and flushing effects at 10 mL/min, which reduce precipitation efficiency. However, further detailed investigation into the intermediate range of flow rates is warranted.

Fig. 4 presents SEM images of precipitates from three experiments, illustrating the characteristics of precipitates in smooth fractures with different apertures. At an aperture of $b = 0.5$ mm, a large fragmented deposit was observed, with one smooth side showing circular shapes, indicating the growth of spherical crystals. As shown in Fig. 4a–b, many spherical crystals appeared as aggregates, surrounded by smaller crystals measuring 1–2 μm. These smaller crystals likely grew on the larger spherical crystals through secondary nucleation. At an aperture of $b = 1$ mm, it is noteworthy that many spherical crystals formed together in a

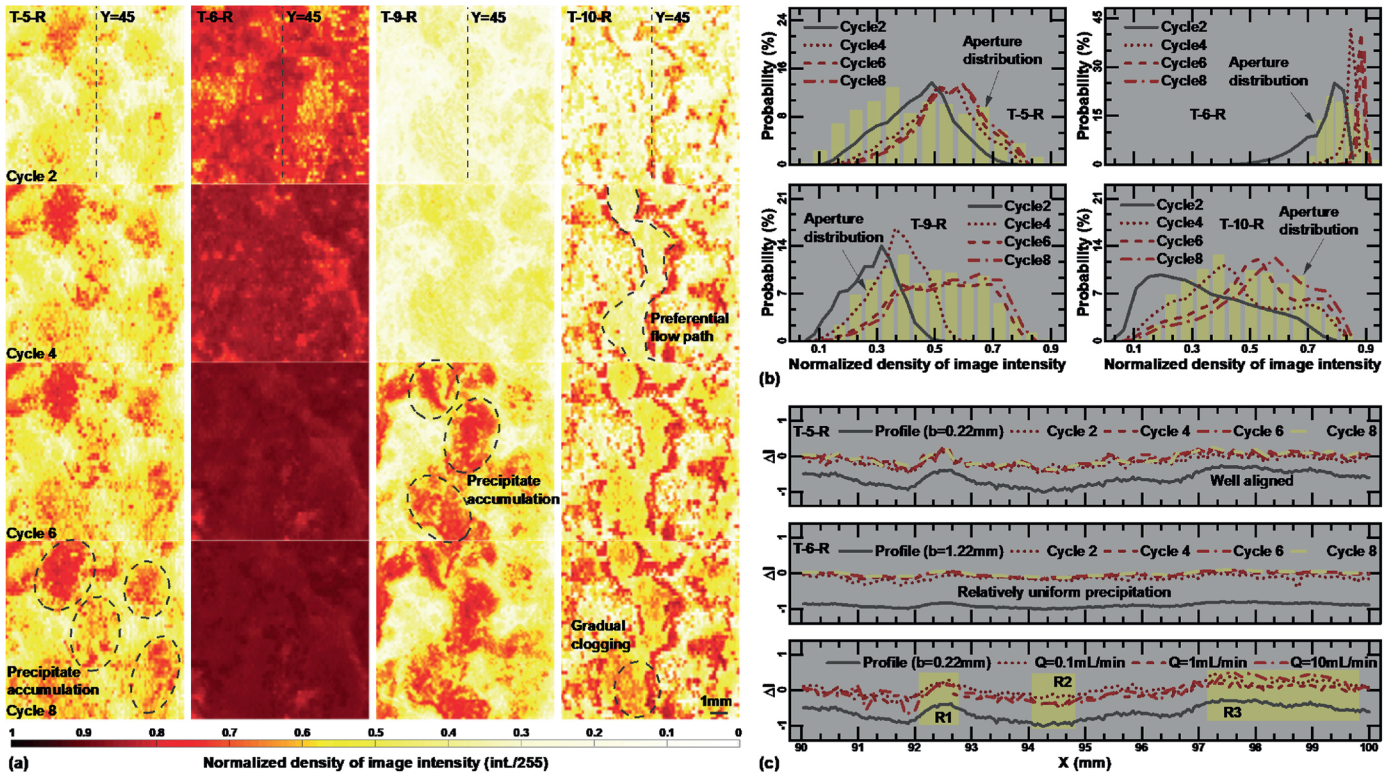

Fig. 5. (a) Colored local precipitation pattern in fractures, (b) Probability distributions of normalized int. and normalized *b*, and (c) Evolution of local precipitation profile in $Y = 45$ mm section.

compact structure, with each crystal measuring 20–50 μm. Crystal competition likely occurred when neighboring crystals came into contact, a phenomenon observed at the microscale (Xiao et al., 2025). Numerous spherical microcrystals are also growing on the surfaces of these larger crystals, as shown in Fig. 4c. When $b = 2$ mm (Fig. 4d), the precipitate morphologies varied, and the crystals were interconnected, forming dense and thick structures. Additionally, many hydrogel-like substances covered the crystal surfaces, possibly residual $CaCl_2$.

To thoroughly investigate the local evolution of biological deposition within macroscale fractures, a central 10 mm × 10 mm region of the fracture was selected. The grayscale images were normalized to a maximum value of 255 and then colorized, as shown in Fig. 5a and supporting Fig. A1 in Appendix A. Higher values indicate greater amounts of precipitation. In rough fractures, Fig. 5a shows the evolution of local precipitation patterns at the end of cycles $n = 2$, 4, 6, and 8. At a narrow aperture of 0.22 mm and a flow rate of 1 mL/min, the amount of precipitation increases with increasing cycles. The precipitation distribution gradually aligns with the local aperture field (Fig. 1a), with more precipitate accumulation occurring in the concave regions. To quantify this evolution, the probability distribution of normalized intensity in the local region is plotted in Fig. 5b, with the background bar graph representing the normalized aperture distribution. The results showed that the distribution of normalized int. closely followed the aperture distribution, and the shape shifts toward the right as the average normalized intensity (I_n^{avg}) increases. This alignment is more apparent at a lower flow rate of 0.1 mL/min, where the probability distribution more closely matches the aperture distribution. At a high flow rate of 10 mL/min, the precipitates do not align well with the aperture field. Instead, a preferential flow path formed, connecting to the concave regions with wider apertures, but gradually became clogged along this path. As a result of higher mass transfer, the probability distribution gradually skews to the right, indicating increased local precipitation. For a wider aperture of 1.22 mm, the precipitation pattern behaves differently. Since the effect of roughness was less pronounced in the wider aperture, the normalized intensity values were higher and more uniformly distributed, showing a clearly right-skewed trend in the probability distribution while still aligning with the aperture distribution. To observe the precipitation profile in the selected local region, a parameter was calculated as $\Delta I = I -$ normalized *b*. The trend of ΔI in the $Y = 45$ mm cross-section and the aperture profile is shown in Fig. 5c. For $b = 0.22$ mm at $Q = 1$ mL/min (T-5-R), it was found that the precipitation profile aligns well with the aperture profile. However, at a wider aperture of 1.22 mm (T-6-R), the precipitation distribution appears more uniform. Regarding the effect of flow rates in rough fractures ($b = 0.22$ mm), the shape of the precipitation profile is more consistent at lower flow rates (0.1 mL/min). In contrast, at a very high flow rate of 10 mL/min, some uneven distribution is observed. Although the precipitate content in the R1 and R2 regions is similar, the higher pore filling fraction in R1 may form a precipitation barrier, similar to what is observed when $X = 97$–100 mm. In smooth fracture, the evolution of local precipitation pattern showed a different performance. As shown in Fig. 5a, the phenomenon of enhanced precipitation was observed at $b = 0.18$ mm as the number of cycles increased. At $b = 0.5$ mm, multiple aggregates formed and eventually developed into a preferential flow path, which later became blocked, as illustrated in Fig. A3a in Appedix A. A wider preferential flow path appeared at $b = 2$ mm, likely because large aggregates, not firmly attached to the fracture surface, were moved by the flow due to low fluid resistance, resulting in a broader flow channel. Overall, the probability shape was more centralized compared to rough

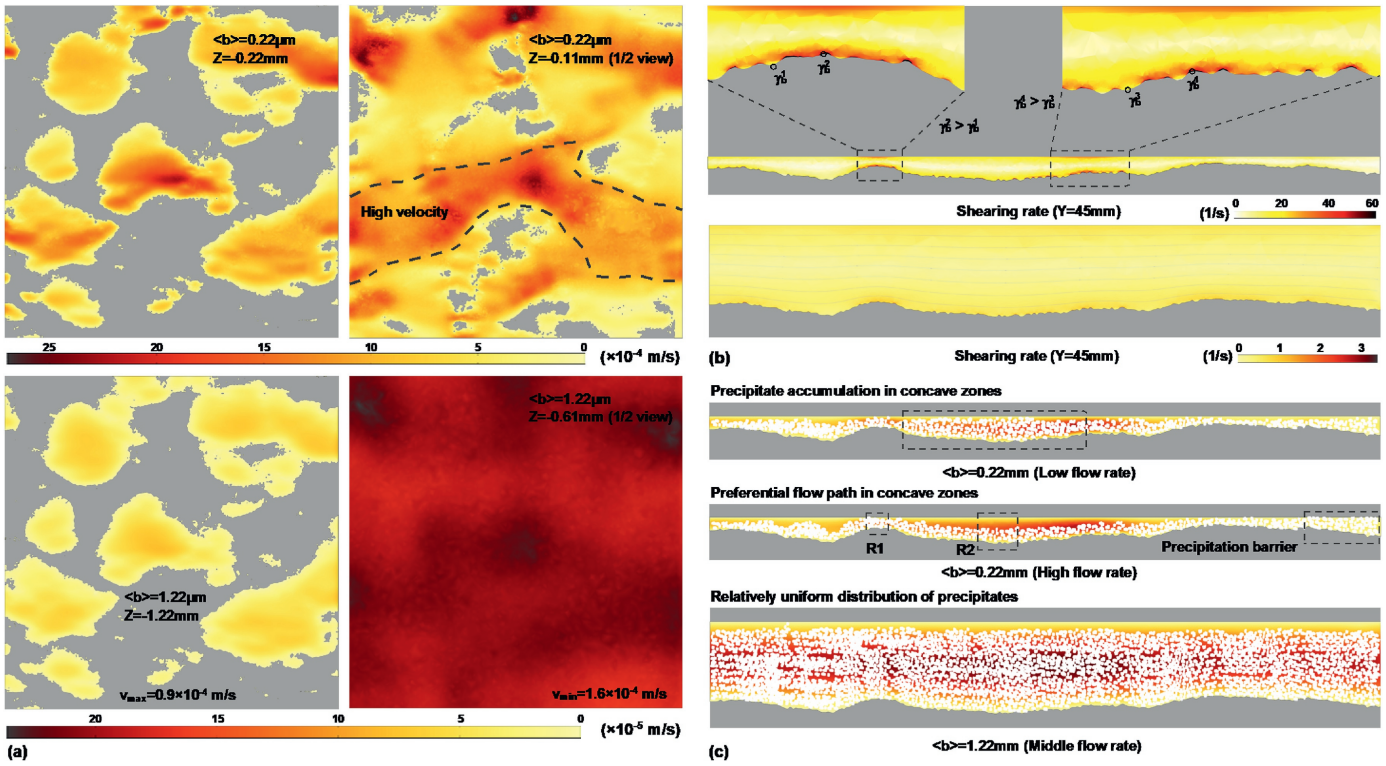

Fig. 6. Numerical simulation characterizations in rough fractures with different apertures: (a) Flow velocity distribution in the *Z*-plane, (b) Shearing rate distribution in the *Y*-plane, and (c) Schematic biologically healing fracture.

fractures (Fig. A3b in Appendix A). The behavior is similar at large apertures in smooth and rough fractures. Additionally, both very low and very high flow rates promoted the formation of individual crystals instead of large precipitation aggregates, resulting in a more uniform distribution compared to that in rough fractures.

To investigate the mechanism behind enzymatically induced precipitation in fracture healing, the initial flow fields in the central selected region of rough fractures with apertures of 0.22 mm and 1.22 mm were simulated using COMSOL Multiphysics. Laminar flow was used to model the flow due to low Reynolds numbers, with an inlet flow rate of 1 mL/min and the outlet set at atmospheric pressure. Symmetry conditions were applied to the lateral boundaries, and other boundaries were treated as no-slip. More details about numerical modeling can be found in the supporting information in Appendix A. The resulting local flow profile is shown in Fig. A4 in Appendix A, and the flow velocity distribution across different cross-sections is presented in Fig. 6a. It can be observed that for a narrow aperture of $b = 0.22$ mm, the flow velocity varies significantly in the vertical direction. Higher velocities are observed in the concave zones, which may result in a preferential flow path at higher flow rates. This is evident in the marked region shown in Fig. 6a, which closely resembles the preferential flow path in Fig. 5a at $Q = 10$ mL/min. The low-velocity region in the convex area could act as a barrier for precipitation, contributing to the formation of flow channels. It agrees with a previous study (Dong et al., 2022), which presumed that the wide preferential flow channels tend to occur in the concave regions. However, this behavior differs from that at lower flow rates, where the shearing rate is minimal, showing small effects on precipitation formation, thus potentially leading to greater precipitates in concave regions, as observed in Fig. 5a and c. The local shearing rate is calculated as $\gamma = \nabla \boldsymbol{u} + (\nabla \boldsymbol{u})^T$ (Bird et al., 2006), and the results are shown in Fig. 6b. It is evident that the shearing rate in the concave region is lower than in the convex region along the flow direction, which promotes precipitate deposition. This uneven distribution of shearing rate leads to localized pressure variations, causing fluid to split into multiple small channels, as evidenced in Fig. 1c and Fig. A1 in Appendix A. Conversely, for a rough fracture of $b = 1.22$ mm, the flow velocity distribution resembles that of a smooth fracture due to the less significant effect of roughness, as illustrated in Fig. 6c. This results in reduced resistance to fluid flow, allowing for a more dispersed flow pattern, and the shearing rate is significantly lower compared to that in the narrower-aperture fracture. This can result in fewer but wider dominant flow branches, as the wider fracture offers a larger cross-sectional area for fluid passing. Conversely, convex regions with narrower apertures tend to form fine flow channels in narrow fractures, as previously reported (Liu et al., 2024).

4. Conclusions and remarks

This study visually explored the application of Enzymatically Induced Carbonate Precipitation (EICP) in transparent fracture models, focusing on the influence of fracture aperture and injection rate on mineral deposition and clogging efficiency. Narrower apertures promote the formation of numerous tortuous flow paths, which gradually become clogged. In contrast, fractures with wider apertures exhibited fewer but wider preferential flow paths, resulting in overall reasonable efficiency. As aperture increases, higher void filling fractions lead to more significant clogging and permeability reduction. The selection of an optimal injection rate is crucial in bioclogging efficiency. Low flow rates cause uneven mineral deposition, particularly inlet clogging. Conversely, excessively high flow rates hinder $CaCO_3$ deposition and adsorption, limiting mineral accumulation and weakening the clogging effect. Image analysis further revealed distinct precipitation patterns

based on fracture surface roughness. In rough fractures, mineral deposition aligns closely with the aperture distribution, forming finger flow in convex zones at low flow rates, while concave zones accumulate more minerals. Higher flow rates result in preferential flow paths within concave zones. In contrast, smooth fractures show more concentrated and random mineral patterns. Overall, one-phase staged EICP shows promise for healing wider-aperture fractures (<2 mm), with moderate injection conditions needing adjustment to optimize EICP for practical applications.

CRediT authorship contribution statement

Yang Xiao: Writing – review & editing, Conceptualization, Funding acquisition. **Chang Zhao:** Formal analysis, Writing – original draft, Investigation, Methodology. **Qingyun Fang:** Data curation, Visualization, Writing – review & editing. **Xiang He:** Writing – original draft, Formal analysis. **Jian Chu:** Methodology, Validation. **Hanlong Liu:** Supervision, Funding acquisition.

Declaration of competing interest

The authors declare that they have no known competing financial interests or personal relationships that could have appeared to influence the work reported in this paper.

Acknowledgments

The authors would like to acknowledge the financial support from the National Natural Science Foundation of China (Grant Nos. 52425806 and 52378325) and the Fundamental Research Funds for the Central Universities (Grant No. 2023CDJKYJH103).

Appendix A. Supplementary data

Supplementary data to this article can be found online at https://doi.org/10.1016/j.jrmge.2025.06.035.

References

Alarifi, S.A., Mustafa, A., Omarov, K., Baig, A.R., Tariq, Z., Mahmoud, M., 2022. A review of enzyme-induced calcium carbonate precipitation applicability in the oil and gas industry. Front. Bioeng. Biotechnol. 10, 900881.

Bird, R.B., Stewart, W.E., Lightfoot, E.N., 2006. Transport Phenomena, second ed. John Wiley & Sons, New York, NY, USA.

Boquet, E., Boronat, A., Ramos-cormenzana, A., 1973. Production of calcite (calcium carbonate) crystals by soil bacteria is a general phenomenon. Nature 246 (5434), 527–529.

Chen, X., Hu, R., Zhou, C., Xiao, Y., Yang, Z., Chen, Y., 2024. Capillary-driven backflow during salt precipitation in a rough fracture. Water Resour. Res. 60 (3), e2023WR035451.

Choi, S.G., Park, S.S., Wu, S., Chu, J., 2017. Methods for calcium carbonate content measurement of biocemented soils. J. Mater. Civ. Eng. 29 (11), 06017015.

Cui, M., Chu, J., Lai, H., 2024. Optimization of one-phase-low-pH enzyme-induced carbonate precipitation method for soil improvement. Acta Geotech. 19 (3), 1611–1625.

Cui, M., Lai, H., Hoang, T., Chu, J., 2022. Modified one-phase-low-pH method for bacteria or enzyme-induced carbonate precipitation for soil improvement. Acta Geotech. 17 (7), 2931–2941.

Cuthbert, M.O., McMillan, L.A., Handley-Sidhu, S., Riley, MichaelS., Tobler, D.J., Phoenix, VernonR., 2013. A field and modeling study of fractured rock permeability reduction using microbially induced calcite precipitation. Environ. Sci. Technol. 47 (23), 13637–13643.

Detwiler, R.L., Pringle, S.E., Glass, R.J., 1999. Measurement of fracture aperture fields using transmitted light: an evaluation of measurement errors and their influence on simulations of flow and transport through a single fracture. Water Resour. Res. 35 (9), 2605–2617.

Dong, Z., Pan, X., Tang, C.S., Shi, B., 2022. Microbial healing of nature-like rough sandstone fractures for rock weathering mitigation. Environ. Earth Sci. 81 (15), 394.

Dullien, F.A.L., 1992. Porous Media: Fluid Transport and Pore Structure, second ed. Academic Press, San Diego, CA, USA.

Handley-Sidhu, S., Sham, E., Cuthbert, M.O., Nougarol, S., Mantle, M., Johns, M.L., Macaskie, L.E., Renshaw, J.C., 2013. Kinetics of urease mediated calcite precipitation and permeability reduction of porous media evidenced by magnetic resonance imaging. Int. J. Environ. Sci. Technol. 10 (5), 881–890.

Hu, J., Xiao, Y., Shi, J., Stuedlein, A.W., Evans, T.M., 2024. Small-strain shear modulus and liquefaction resistance of calcareous sand with non-plastic fines. Geotechnique 1–15.

Lai, H., Cui, M.J., Chu, J., 2023a. Effect of pH on soil improvement using one-phase-low-pH MICP or EICP biocementation method. Acta Geotech 18 (6), 3259–3272.

Lai, H., Cui, M., Wu, S., Yang, Y., Chu, J., 2023b. Extraction of crude soybean urease using ethanol and its effect on soil cementation. Soils Found. 63 (3), 101300.

Lioliou, M.G., Paraskeva, C.A., Koutsoukos, P.G., Payatakes, A.C., 2007. Heterogeneous nucleation and growth of calcium carbonate on calcite and quartz. J. Colloid Interface Sci. 308 (2), 421–428.

Liu, Q., Zhang, B., Wang, J., Sun, Z., Peng, Z., Wang, J., Wang, H., 2024. Microbially mediated rock fine fracture mineralization sealing: evolution of flow channels and the resulting transmissivity reduction. Eng. Geol. 334, 107525.

Minto, J.M., Hingerl, F.F., Benson, S.M., Lunn, R.J., 2017. X-ray CT and multiphase flow characterization of a 'bio-grouted' sandstone core: the effect of dissolution on seal longevity. Int. J. Greenh. Gas Control 64, 152–162.

Minto, J.M., MacLachlan, E., El Mountassir, G., Lunn, R.J., 2016. Rock fracture grouting with microbially induced carbonate precipitation. Water Resour. Res. 52 (11), 8827–8844.

Mountassir, G.E., Lunn, R.J., Moir, H., MacLachlan, E., 2014. Hydrodynamic coupling in microbially mediated fracture mineralization: formation of self-organized groundwater flow channels. Water Resour. Res. 50 (1), 1–16.

Mukhopadhyay, M., Dalvi, S.V., 2005. Analysis of supersaturation and nucleation in a moving solution droplet with flowing supercritical carbon dioxide. J. Chem. Technol. Biotechnol. 80 (4), 445–454.

Neretnieks, I., 2007. Single Well Injection Withdrawal Tests (SWIW) in Fractured Rock - Some Aspects on Interpretation. Swedish Nuclear Fuel and Waste Management Co., Sweden.

Peng, S., Di, H., Fan, L., Fan, W., Qin, L., 2020. Factors affecting permeability reduction of micp for fractured rock. Front. Earth Sci. 8, 217.

Phillips, A.J., Cunningham, A.B., Gerlach, R., Hiebert, R., Hwang, C., Lomans, B.P., Westrich, J., Mantilla, C., Kirksey, J., Esposito, R., Spangler, L., 2016. Fracture sealing with microbially-induced calcium carbonate precipitation: a field study. Environ. Sci. Technol. 50 (7), 4111–4117.

Ran, D., Kawasaki, S., 2016. Effective use of plant-derived urease in the field of geoenvironmental/geotechnical engineering. J. Civ. Environ. Eng. 6 (1), 1000207.

da Rocha Gomes, S., Ferrara, L., Sánchez, L., Moreno, M.S., 2023. A comprehensive review of cementitious grouts: composition, properties, requirements and advanced performance. Constr. Build. Mater. 375, 130991.

Song, Z., Wu, C., Li, Z., Shen, D., 2024. Fracture sealing based on microbially induced carbonate precipitation and its engineering applications: a review. Biogeotechnics 2 (4), 100100.

Tobler, D.J., Minto, J.M., El Mountassir, G., Lunn, R.J., Phoenix, V.R., 2018. Microscale analysis of fractured rock sealed with microbially induced $CaCO_3$ precipitation: influence on hydraulic and mechanical performance. Water Resour. Res. 54 (10), 8295–8308.

Viswanathan, H.S., Ajo-Franklin, J., Birkholzer, J.T., Carey, J.W., Guglielmi, Y., Hyman, J.D., Karra, S., Pyrak-Nolte, L.J., Rajaram, H., Srinivasan, G., Tartakovsky, D.M., 2022. From fluid flow to coupled processes in fractured rock: recent advances and new frontiers. Rev. Geophys. 60 (1), e2021RG000744.

Wang, Y., Soga, K., DeJong, J.T., Kabla, A.J., 2019a. Microscale visualization of microbial-induced calcium carbonate precipitation processes. J. Geotech. Geoenviron. Eng. 145 (9), 04019045.

Wang, Y., Soga, K., Dejong, J.T., Kabla, A.J., 2019b. A microfluidic chip and its use in characterising the particle-scale behaviour of microbial-induced calcium carbonate precipitation (MICP). Geotechnique 69 (12), 1086–1094.

Wang, Y., Soga, K., DeJong, J.T., Kabla, A.J., 2021. Effects of bacterial density on growth rate and characteristics of microbial-induced caco3 precipitates: particle-scale experimental study. J. Geotech. Geoenviron. Eng. 147 (6), 04021036.

Weinhardt, F., Class, H., Vahid Dastjerdi, S., Karadimitriou, N., Lee, D., Steeb, H., 2021. Experimental methods and imaging for enzymatically induced calcite precipitation in a microfluidic cell. Water Resour. Res. 57 (3), e2020WR029361.

Whiffin, V.S., 2004. Microbial CaCO3 Precipitation for the Production of Biocement. PhD Thesis. Morduch University, Perth, West Australia.

Wu, C., Chu, J., Wu, S., Cheng, L., van Paassen, L.A., 2019a. Microbially induced calcite precipitation along a circular flow channel under a constant flow condition. Acta Geotech 14 (3), 673–683.

Wu, C., Chu, J., Wu, S., Guo, W., 2019b. Quantifying the permeability reduction of biogrouted rock fracture. Rock Mech. Rock Eng. 52 (3), 947–954.

Wu, C., Chu, J., Wu, S., Hong, Y., 2019c. 3D characterization of microbially induced carbonate precipitation in rock fracture and the resulted permeability reduction. Eng. Geol. 249, 23–30.

Xiao, P., Liu, H., Stuedlein, A.W., Evans, T.M., Xiao, Y., 2019. Effect of relative density and biocementation on cyclic response of calcareous sand. Can. Geotech. J. 56 (12), 1849–1862.

Xiao, P., Liu, H., Xiao, Y., Stuedlein, A.W., Evans, T.M., 2018. Liquefaction resistance of bio-cemented calcareous sand. Soil Dynam. Earthq. Eng. 107, 9–19.

Xiao, Y., He, X., Ma, G., Zhao, C., Chu, J., Liu, H., 2024. Biomineralization and mineralization using microfluidics: a comparison study. J. Rock Mech. Geotech. Eng. 16 (2), 661–669.

Xiao, Y., He, X., Zaman, M., Ma, G., Zhao, C., 2022a. Review of strength improvements of biocemented soils. Int. J. GeoMech. 22 (11), 03122001.
Xiao, Y., Ma, G., Wu, H., Lu, H., Zaman, M., 2022b. Rainfall-induced erosion of biocemented graded slopes. Int. J. GeoMech. 22 (1), 04021256.
Xiao, Y., He, X., Stuedlein, A.W., Chu, J., Matthew Evans, T., van Paassen, L.A., 2022c. Crystal growth of micp through microfluidic chip tests. J. Geotech. Geoenviron. Eng. 148 (5), 06022002.
Xiao, Y., Zhao, C., Cui, H., Chen, Y., Wu, B., Liu, H., 2025. Microscale insights into enzyme-induced carbonate precipitation in rock-based microfluidic chips. Geotechnique 75 (7), 846–857.
Zhang, J., Xiao, Y., Liu, H., Chu, J., 2025. Role of bacteria on bio-induced calcium carbonate formation: insights from droplet microfluidic experiments. Geotechnique 75 (6), 787–799.
Zhao, C., Xiao, Y., Chu, J., Hu, R., Liu, H., He, X., Liu, Y., Jiang, X., 2023. Microfluidic experiments of biological CaCO3 precipitation in transverse mixing reactive environments. Acta Geotech. 18 (10), 5299–5318.
Zhao, C., Xiao, Y., He, X., Cui, H., Liu, H., 2024. EICP-enhanced fracture healing: bridging microfluidic observations and macroscale applications. Geotechnique 1–13.
Zhao, C., Xiao, Y., He, X., Liu, H., Liu, Y., Chu, J., 2025a. Influence of injection methods on bio-mediated precipitation of carbonates in fracture-mimicking microfluidic chip. Geotechnique 75 (2), 153–165.
Zhao, C., Xiao, Y., Liu, H., Chu, J., 2025b. Effects of urease and cementing solution concentrations on micro-scale enzymatic mineralisation characteristics. Geotechnique 75 (6), 732–746.
Zhao, Y., Xiao, Z., Fan, C., Shen, W., Wang, Q., Liu, P., 2020. Comparative mechanical behaviors of four fiber-reinforced sand cemented by microbially induced carbonate precipitation. Bull. Eng. Geol. Environ. 79 (6), 3075–3086.
Zhu, C., Li, Z., Zhang, Z., Zhang, Y., Zhou, Y., Wang, J., 2023. Increased content and uniformity of enzyme-induced calcite precipitation realized by prehydrolysis and an accelerated injection rate. Front. Earth Sci. 11, 1249295.
Zimmerman, R.W., Al-Yaarubi, A., Pain, C.C., Grattoni, C.A., 2004. Non-linear regimes of fluid flow in rock fractures. Int. J. Rock Mech. Min. Sci. 41 (3), 384.

Dr. Yang Xiao was the “China Highly Cited Scholar" for a seventh consecutive year and was awarded with one national second prize, two first awards of ministerial or provincial science and technology. He is also a three-time recipient of the Fredlund Award from the Canadian Geotechnical Society. He has published more than 170 papers in reputable journals. Dr. Xiao was the associate editor of *International Journal of Geomechanics* (ASCE), and *Canadian Geotechnical Journal*, etc., and the executive deputy Editor-in-Chief of *Biogeotechnics*. The research group headed by Dr. Xiao has made some achievements in the fields of bacterial-scale mechanism of bio-mineralization, grain-scale and element-scale mechanisms of bio-treated soils, constitutive theory of bio-cemented soils, and field-scale bio-treatment method.